

Molecular insights into receptor binding energetics and neutralization of SARS-CoV-2 variants

Melanie Koehler

Université catholique de Louvain

Ankita Ray

Université catholique de Louvain

Rodrigo Azevedo Moreira da Silva

Polish Academy of Sciences <https://orcid.org/0000-0002-7605-8722>

Blinera Juniku

Université catholique de Louvain

Adolfo Poma

Institute of Fundamental Technological Research, Polish Academy of Sciences <https://orcid.org/0000-0002-8875-3220>

David Alsteens (✉ David.Alsteens@uclouvain.be)

Université Catholique de Louvain <https://orcid.org/0000-0001-9229-113X>

Article

Keywords: SARS-CoV-2, ACE2, RBD, Variant, VoC, force, binding, AFM, atomic force microscopy, molecular dynamics simulation, energy, structure, neutralization, antibody

Posted Date: August 13th, 2021

DOI: <https://doi.org/10.21203/rs.3.rs-764098/v1>

License:   This work is licensed under a Creative Commons Attribution 4.0 International License.

[Read Full License](#)

Version of Record: A version of this preprint was published at Nature Communications on November 30th, 2021. See the published version at <https://doi.org/10.1038/s41467-021-27325-1>.

24 **ABSTRACT**

25 Despite an unprecedented global gain in knowledge since the emergence of SARS-CoV-2,
26 almost all mechanistic knowledge related to the molecular and cellular details of viral
27 replication, pathology and virulence has been generated using early prototypic isolates of
28 SARS-CoV-2. Here, using atomic force microscopy and molecular dynamics, we investigated
29 how these mutations quantitatively affected the kinetic, thermodynamic and structural
30 properties of RBD—ACE2 complex formation. We observe a direct link between increased
31 RBD—ACE2 complex stability and the greater transmissibility observed for the variants of
32 concern. While the N501Y and E484Q mutations are particularly important for the greater
33 stability, the N501Y mutation is unlikely to significantly affect antibody neutralization. This
34 work provides unprecedented atomistic detail on the binding of SARS-CoV-2 variants and
35 provides insight into the impact of viral mutations on infection-induced immunity.

36 INTRODUCTION

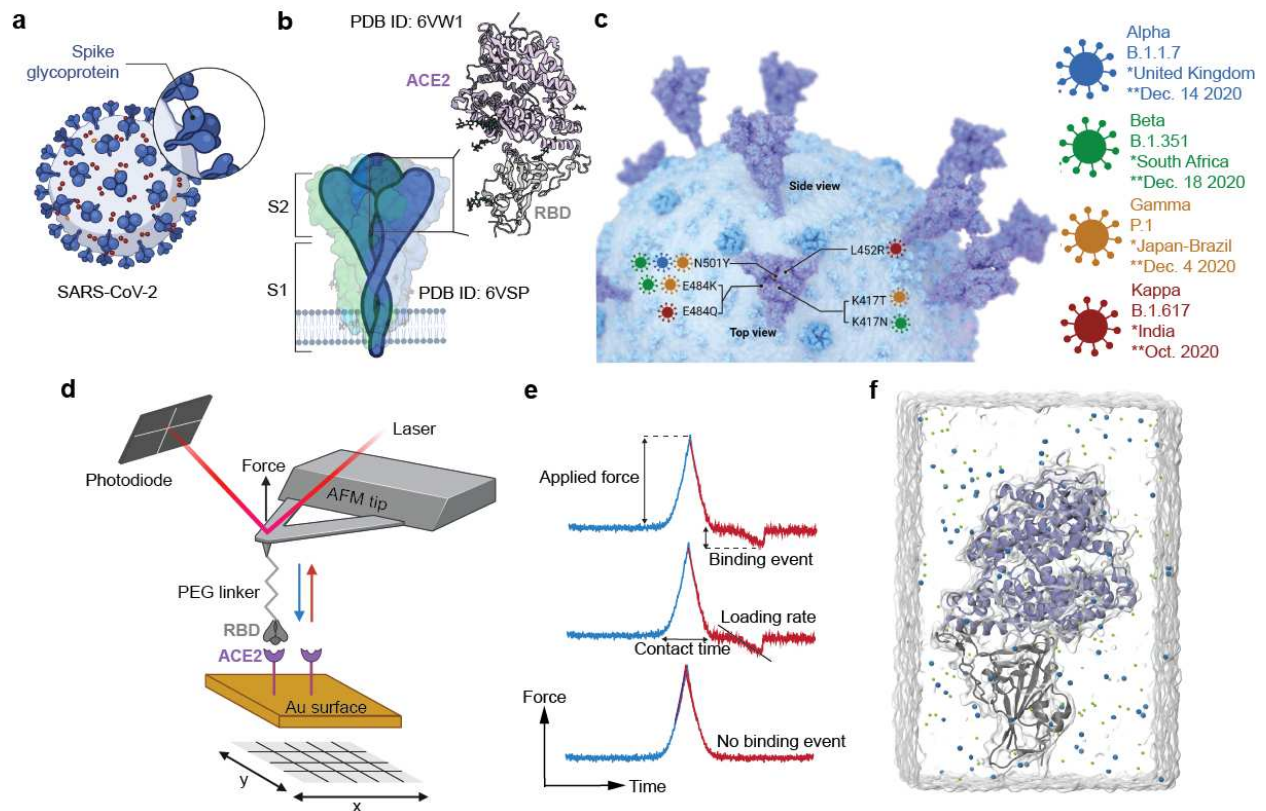
37 One and half year since the start of the COVID-19 pandemic, we are just beginning to
38 understand how the severe acute respiratory syndrome novel coronavirus (SARS-CoV-2) can
39 overcome host cell entry barriers and outsmart the human immune response^{1,2}. Fortunately,
40 several vaccines have been developed that can currently prevent COVID-19 with high efficacy,
41 and their roll out is expected to help control the pandemic³. However, with little more than
42 10% of the world population presently (July 2021) vaccinated, the continuous emergence of
43 SARS-CoV-2 variants with reduced susceptibility to infection- and vaccine-induced immunity,
44 and the vast animal reservoir of SARS-like viruses, there is no time for complacency⁴. Rapidly
45 spreading SARS-CoV-2 variants of concern (VoCs) demonstrate how easily this virus can
46 accommodate antigenic changes in its spike protein without any loss of fitness⁵.

47 Despite an unprecedented global gain in knowledge since the surge of SARS-CoV-2, almost all
48 mechanistic insights related to molecular and cellular details of viral replication, pathology
49 and virulence have been generated using prototypic early SARS-CoV-2 isolates (such as the
50 original Wuhan isolate). Unexpectedly, however, SARS-CoV-2 evolved into a moving target
51 with VoC, such as the infamous Indian variants (Kappa and Delta), and Variants of Interest
52 collectively now representing over 90% of GISAID sequence entries⁶. As for all viruses, entry is
53 a key step in the SARS-CoV-2 life cycle. The receptor-binding motif (RBM), which is part of the
54 receptor-binding domain (RBD) localized at the top of the trimeric SARS-CoV-2 spike (**Fig. 1a,**
55 **b**), is a prime target for neutralizing antibodies that are induced by infection or by currently
56 used COVID-19 vaccines⁷. The RBM is responsible for binding angiotensin converting enzyme
57 2 (ACE2) as primary receptor for the virus (**Fig. 1b**). The RBM, however, is very tolerant to
58 mutations (**Fig. 1c**), many of which do not affect or even enhance human ACE2 receptor
59 binding but may be detrimental for antibody recognition. N501Y, for example, present in the

60 Alpha, Beta, and Gamma variants, increases ACE2 binding^{8,9}. One of the far-reaching
61 consequences of this antigenic variation of the RBM was the withdrawal of Eli Lilly's
62 monoclonal antibody bamlanivimab from emergency use approval as monotherapy for the
63 treatment of COVID-19 patients, because VoCs with E484K/Q mutations had become
64 resistant. Current knowledge, despite all the enormous efforts, threatens to be outdated if
65 not anticipating on future evolutions, therefore a better understanding on the impact of spike
66 protein mutations on the spike-receptor interaction at atomic resolution is of pivotal
67 importance as well as its influence on its inhibition by antibodies.

68 Previously, we have reported the use of atomic force microscopy (AFM) to map the interaction
69 forces between the AFM tips functionalized with the S-glycoprotein of RBD wildtype (WT) and
70 the ACE2 receptors on model surfaces. By single-molecule force spectroscopy (SMFS) and
71 bilayer interferometry (BLI), we have shown that there is a high affinity (~ 120 nM) guided
72 by specific multivalent interactions at the RBD/ACE2 interface¹⁰. In this study, by using force-
73 distance (FD) curve-based atomic force microscopy, we have derived the kinetic and
74 thermodynamic parameters between the ACE2 receptors on model surface with RBD of four
75 different SARS-CoV-2 mutants (Alpha, Beta, Gamma, and Kappa respectively) (**Fig. 1c-e**). In
76 addition to single molecule force spectroscopy, we also elucidated the molecular basis of
77 increased transmissibility. In this regard all-atom molecular dynamics (MD) simulation has
78 been employed to characterize the energetic and structural changes for the RBD—ACE2
79 complex interface. Thus, the monitoring of Lennard-Jones and electrostatic energies and the
80 strength of residue contacts established at the interface provide a good description of local
81 and long-range effects caused by mutations. Alpha, Beta, Gamma and Kappa VoCs share
82 common mutations which affect the close environment of the mutated amino acids.
83 Furthermore, some residue contacts far away from those amino acids vary towards high

84 strengths (or frequencies in MD) which induce an effect of structural stabilization, in particular
85 for Gamma and Kappa mutants. Finally, we tested the neutralization efficiency of two mAbs,
86 obtained by immunization of a mouse with the WT-RBD. Strikingly, we observed that one mAb
87 shows excellent anti-binding properties against all variant while the second tested one lost its
88 neutralization potential for the three variants having the E484 mutation.



90

91 **Figure 1 | SARS-CoV-2 mutant binding to ACE2 host receptor quantified by atomic force microscopy (d, e) and**
 92 **molecular dynamics simulation (f).** (a) Schematic of a SARS-CoV-2 virus particle, expressing at its surface the
 93 spike glycoprotein (S) that mediates the binding to host cells. (b) The S glycoprotein is composed of two subunits,
 94 S1 and S2, and is commonly represented as a sword-like spike. The Protein Data Bank (PDB) model of this
 95 glycoprotein (ID: 6VSP) reveals how the subunits are comprised of different regions that are fundamental to the
 96 infection process. Other Structural studies (PDB ID: 6VW1) have previously obtained a complex between the
 97 receptor-binding domain (RBD, a subunit of the S glycoprotein) and the angiotensin-converting enzyme 2 (ACE2)
 98 receptor. (c) Featuring a 3D rendering of SARS-CoV-2, this panel showcases the key spike protein mutations in
 99 the RBD domain on each of the studied SARS-CoV-2 variants of concern: Alpha, Beta, Gamma and Kappa. (d)
 100 Schematic of probing RBD mutant binding to ACE2 receptors using atomic force microscopy (AFM). RBD is
 101 covalently attached to the AFM tip via a heterobifunctional PEG-linker and their binding to ACE2 receptors
 102 immobilized on a gold (Au) coated surface is probed. Pixel-for-pixel force distance (FD) curve-based AFM
 103 approaches and retracts the tip of an AFM cantilever from the sample to record interaction forces, F , over the
 104 tip-sample distance in FD curves. (e) Force-time curve from which the loading rate (LR) can be extracted from
 105 the slope of the curve just before bond rupture ($LR = \Delta F / \Delta t$) (upper curve). The contact time refers to the time
 106 when the tip and surface are in constant contact (middle curve). The lower curve shows no binding event. (f)
 107 Representation of the system used in MD simulations.

108 **RESULTS**

109 **VoCs RBD binding to ACE2 is facilitated.**

110 Several mechanisms might account for increased variant transmissibility, such as increased
111 spike protein density, greater furin cleavage accessibility and enhanced spike protein binding
112 affinity for the ACE2 receptor^{11,12}. To test whether the VoCs bind ACE2 with an increased
113 affinity, binding of purified Alpha-, Beta-, Gamma- and Kappa-RBD were compared with
114 binding of the WT-RBD, using FD-curve based AFM. To mimic cell-surface receptors *in vitro*,
115 ACE2 receptors were covalently immobilized via NHS/EDC chemistry on OH-/COOH-
116 terminated alkanethiol grafted gold-coated surfaces (see Methods). The various VoC RBD
117 proteins were covalently attached to the free end of a long, polyethylene glycol (PEG)₂₄ linker
118 linked to the AFM tip^{10,13} (**Fig. 1d**). To investigate the binding potential, the RBD modified tips
119 were cyclically approached and retracted from the ACE2 surface. The force acting between
120 the functionalized tip and the surface [expressed in piconewtons (pN)] was monitored over
121 time, resulting in force vs. time curves (**Fig. 1e**)^{13,14}. Upon retraction, binding events were
122 commonly observed at rupture distances >12 nm (corresponding to the full extension of the
123 PEG linker and use as a signature of specific unbinding events), with binding frequencies as
124 follows: Alpha-RBD \approx Beta-RBD \approx Gamma-RBD \approx Kappa-RBD > WT-RBD (**Fig. 2a**). The specificity
125 of these interactions was confirmed by control experiments using (i) an AFM tip only
126 functionalized with the PEG linker or (ii) toward NHS/EDC surfaces missing the receptor.
127 **Supplementary Fig. 1** shows a significant decrease in adhesion when the RBD strain was
128 absent or when the interaction was studied between the RBD functionalized AFM tip and
129 receptor lacking surface, confirming that the vast majority of the recorded binding events
130 stemmed from specific interactions. The binding frequencies are in good agreement with the
131 data previously reported for the WT-RBD using the same approach¹⁰. For the VoCs, the higher

132 binding frequencies observed suggest that their binding to ACE2 are facilitated in comparison
133 to the WT, which is in good agreement with the higher transmissibility observed of those VoCs.

134 **Thermodynamics of VoCs-RBD—ACE2.**

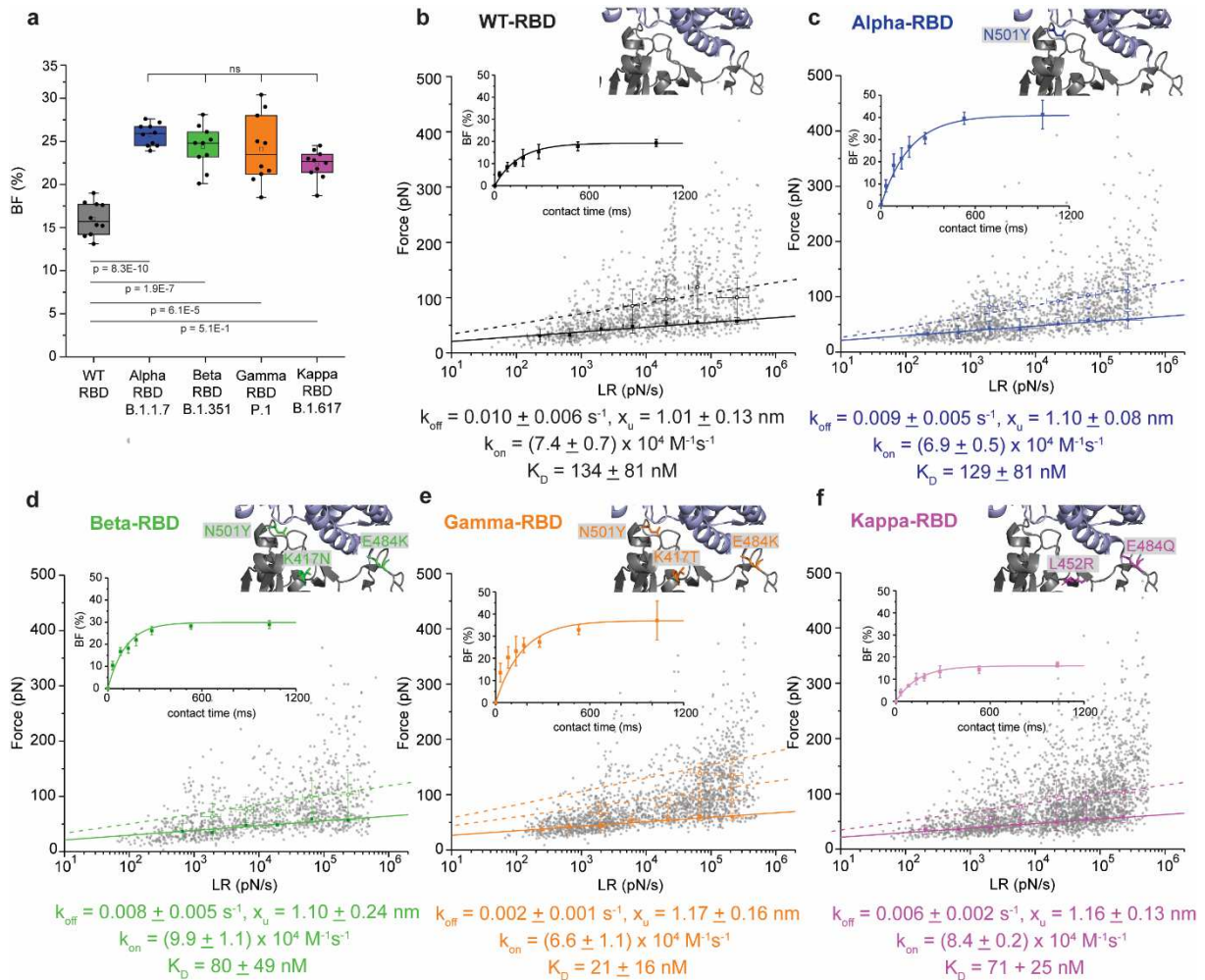
135 Having shown that VoCs have a higher binding potential, we then investigated whether this
136 difference could originate from a higher binding affinity at the single-molecule level. Using FD-
137 based AFM, we measured the strength of the RBD-ACE2 complexes by applying an external
138 force (F) on the bond and extracted the kinetics properties of the interaction using the Bell-
139 Evans model^{15,16}, which predicts that far from equilibrium, the binding strength of the ligand-
140 receptor bond scales linearly with the logarithm of the loading rate (LR, force load on the bond
141 over time) . Experimentally, FD curves were recorded at various retraction speeds (**Fig. 2b-f**)
142 and hold times (**Fig. 2b-f**, inserts) and plotted in so called dynamic force spectroscopy (DFS),
143 showing the force vs LR. WT-RBD (**Fig. 2b**, black), Alpha-RBD (**Fig. 2c**, blue), Beta-RBD (**Fig. 2d**,
144 green), Gamma-RBD (**Fig. 2e**, orange) and Kappa-RBD (**Fig. 2f**, purple) binding towards
145 immobilized ACE2 receptors were analyzed, revealing that all complexes withstood forces
146 between 25 and 400 pN over the range of applied LRs (N > 2500 data points for each complex),
147 in good agreement with the previously forces measured for the interactions probed between
148 WT-S1—ACE2 and WT-RBD—ACE2¹⁰ and for other virus-receptor bonds^{14,17-20}. Although
149 forces in this range can affect conformational stability of proteins, RBD proteins remained
150 mechanically stable as evidenced by control experiments, showing thousands of stable
151 interactions over several scans. Forces measured at different LRs were thoroughly analyzed
152 and plotted in DFS plots (**Fig. 2b-f**), as established previously^{10,14,19} (see methods and
153 **Supplementary Fig. 2-6**). Since single interactions were predominantly taking place, the data
154 was fitted with the Bell-Evans model, and k_{off} and x_u were extracted for the probed interaction
155 pairs. Similar distances to the transition state were observed for either the WT-RBD or the

156 VoCs-RBD interacting with the ACE2 receptor, indicating a similar binding geometry/ location
157 of the binding pocket under these conditions. However, a decrease in the dissociation rate
158 extrapolated to zero force was detected for the RBD mutants in the following order: WT-RBD
159 ($k_{\text{off}} = 0.010 \pm 0.006 \text{ s}^{-1}$) > Alpha-RBD \approx Beta > Kappa > Gamma, with the Kappa and Gamma
160 forming twofold and fivefold more stable complexes, respectively. Accordingly, the lifetime τ
161 of a single molecule bond can be directly obtained from the k_{off} ($\tau = k_{\text{off}}^{-1}$), resulting in a bond
162 lifetime of $\approx 100\text{ms}$ for WT and Alpha-RBD—ACE2 complexes, $\approx 125 \text{ ms}$ for Beta, $\approx 165 \text{ ms}$ for
163 Kappa, and $\approx 500 \text{ ms}$ for Gamma. Higher forces observed on the DFS plots originate from the
164 failure of uncorrelated bonds in parallel, as predicted by the Williams-Evans prediction. We
165 observed a good correlation between the William-Evans prediction and the single-molecule
166 data recorded. This observation underlines the important role of multivalency during virions
167 attachment to cell surface receptors. The high density of RBDs on virions (on the trimeric
168 spikes and this one replicated many times on the virion surface), favors the establishment of
169 multiple bonds towards an enhanced apparent lifetime of the virus-host interaction.

170 At the single-molecule level, a more accurate picture of the overall bond lifetime can be
171 obtained by the dissociation constant K_D of the complex. For instance, high-affinity
172 interactions have a long lifetime as K_D is defined as the ratio between k_{off} and the kinetic on-
173 rate of the complex formation (k_{on}). Experimentally, by assuming that the receptor-bond
174 complex formation can be approximated by a pseudo-first-order kinetics, k_{on} can be extracted
175 from the binding frequency (BF) measured at various hold times (**Fig. 2b-f**, inserts). This
176 association rate depends on the effective concentration c_{eff} , described as the number of
177 binding partners (RBD protein + ACE2 receptor) within an effective volume V_{eff} accessible
178 under free-equilibrium conditions. We approximated V_{eff} by a half-sphere with a radius
179 including the linker, RBD protein and ACE2 receptor. For all the studied interaction pairs, we

180 saw an exponential increase in the BF over time, and calculated their k_{on} , after extracting the
181 interaction time. Collectively, these experiments lead to the following calculated equilibrium
182 dissociation constants K_D (k_{off}/k_{on}) in ascending order: Gamma ($K_D = 21 \pm 16$ nM) < Kappa (K_D
183 $= 71 \pm 25$ nM) \approx Beta ($K_D = 80 \pm 49$ nM) < Alpha ($K_D = 129 \pm 81$ nM) \approx WT ($K_D = 134 \pm 81$ nM).
184 All these K_D correspond to high affinity interactions, confirming the high-affinity and stability
185 of the complexes established by SARS-CoV-2 with its cognate ACE2 receptor. Especially the
186 Gamma variant as well as the Kappa and Beta ones show significantly lower K_D values
187 compared to the WT complex. Other interaction studies between RBD WT and ACE2, as well
188 as between SARS-CoV (80% sequence homology) and ACE2 reported specific, high-affinity
189 association values in the nM range.^{10,21}

190 Taken together, our *in vitro* experiments show that the four investigated VoCs, having
191 emerged, show higher binding properties to ACE2 receptors, both in terms of affinity and
192 stability. K_D values observed in this nM range imply a very strong affinity and specificity,
193 making the development of anti-binding molecules targeting this interaction, such as
194 antibodies, more difficult. The continuous appearance of VoCs seems to be an evolution
195 towards complexes of higher stability while inserting key point mutations that could escape
196 neutralization by convalescent sera or vaccine-derived sera.



197

198

199

200

201

202

203

204

205

206

207

208

209

210

211

212

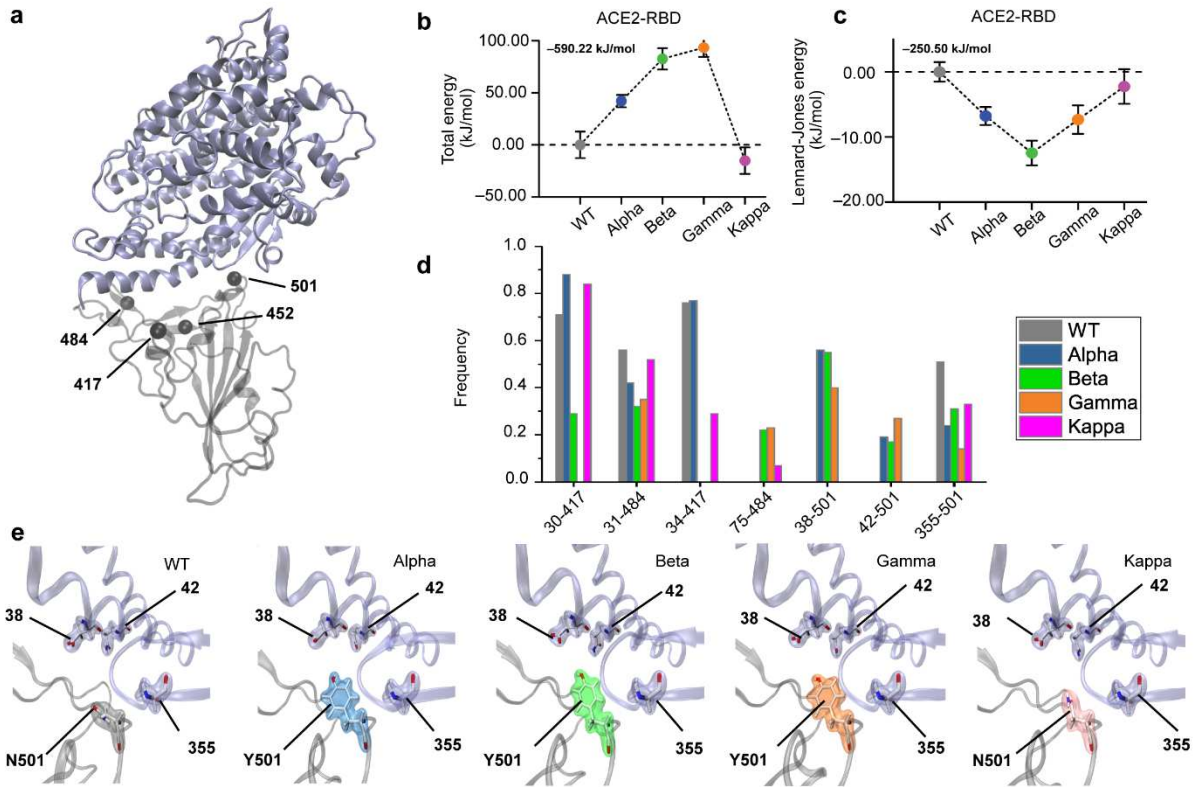
213

214

Figure 2 | RBD mutant avidity for its ACE2 host receptor quantified by AFM. (a) Box plot of specific binding frequencies (BF) measured by AFM between the functionalized tip (RBD mutants) and the grafted ACE2 model surface. One data point belongs to the BF from one map acquired at $1 \mu\text{m/s}$ retraction speed and 250 ms contact time. The square in the box indicates the mean, the colored box the 25th and 75th percentiles, and the whiskers the highest and lowest values of the results. The line in the box indicates the median. $N = 10$ maps examined over 3 independent experiments. P-values were determined by the two-sample t test in Origin. (b-f) Dynamic force spectroscopy (DFS) plot showing the individual force extracted from individual F-D curves (grey data points) as well as the average rupture forces, determined at seven distinct loading rate (LR) ranges measured either between ACE2 receptor and WT-RBD (b), Alpha-RBD (c), Beta-RBD (d), Gamma-RBD (e) or Kappa-RBD (f). Data corresponding to single interactions were fitted with the Bell-Evans (BE) model (straight line), providing average k_{off} and x_u values. Dashed lines represent predicted binding forces for multiple simultaneous uncorrelated interactions ruptured in parallel (Williams-Evans [WE] prediction). **Inserted plots:** The binding frequency (BF) is plotted as a function of the contact time. Least-squares fits of the data to a mono-exponential decay curve (line) provides average kinetic on-rates (k_{on}) of the probed interaction. Further calculation (k_{off}/k_{on}) leads to K_D . One data point belongs to the BF from one map acquired at $1 \mu\text{m/s}$ retraction speed for the different contact times. All experiments were reproduced at least three times with independent tips and samples. The error bars indicate s.d. of the mean value.

215 **Dynamics and structural stability of ACE2-RBD complexes**

216 To elucidate the molecular mechanism underlying the higher stability of RBD-ACE2 complexes
217 observed for VoCs, we performed MD simulations. A cumulative 7.5 μ s of all-atom MD
218 simulation of fully solvated RBD—ACE2 complexes (**Fig. 3a**) were performed using the
219 GROMACS package²². Standard modelling of WT and VoC systems as well as MD simulation
220 protocols are reported in the Method section. Briefly, after the energy minimization step and
221 equilibration of the simulation box, 5 replicas with 250 ns of unconstrained MD simulation for
222 each system were performed and analyzed. The various RBD—ACE2 complexes were dynamic
223 but remained stably bound throughout each simulation, as shown by C α root mean square
224 deviation (RMSD) from the starting equilibrated structure that was less than 10 Å for each RBD
225 tested.



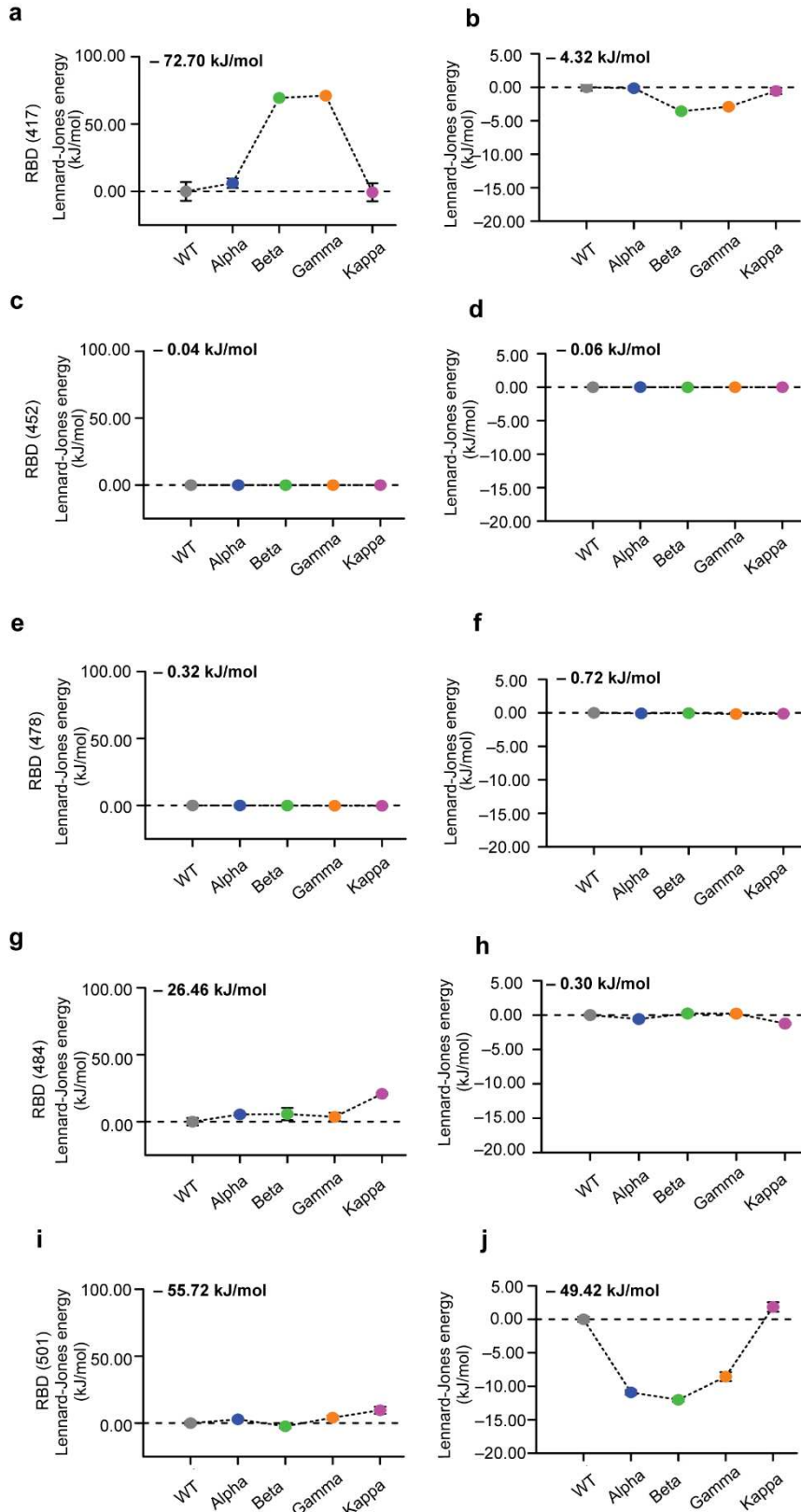
226

227 **Figure 3 | MD simulation of the RBD—ACE2 of WT and VoCs.** (a) Ribbon-like representation of the RBD—ACE2
 228 complex and highlight of residues mutated in VoCs. (b) Total energies and (c) Lennard-Jones energies for all
 229 RBD—ACE2 complexes. (d) Average frequencies of contacts from 7.5 μ s of MD trajectory of SARS-CoV-2 WT
 230 (black) and VoCs Alpha (green), Beta (blue), Gamma (orange), and Kappa (purple). High-frequency contacts are
 231 shown in the form (ACE2 residue number) - (RBD residue number) for 7 contacts involving relevant mutations.
 232 (e) Zoom-in on the RBD—ACE2 region around RBD residue 501 for the WT and the 4 VoCs. Sidechains are
 233 represented by sticks. Residues 38, 42 and 355 in ACE2 contacting RBD residue 501 are shown.
 234

235 In the first step, we compared the total energy of the RBD—ACE2 complexes. For the WT
236 complex, the potential energy between the RBD and ACE2, which is the summation of the
237 intermolecular long-range Coulomb and Lenard-Jones interactions, showed an energy around
238 -590.22 kJ/mol, in good agreement with previously published data^{23,24}. Surprisingly, only the
239 Kappa variant, among the four VoCs studied, showed a more stable binding complex with a
240 decrease of the total energy of 15.2 kJ/mol (**Fig. 3b**). By looking at the interfacial energy, we
241 observed on the contrary that only the three other VoCs (Alpha, Beta, Gamma) show a gain in
242 the Lennard-Jones energy of around 10 kJ/mol below the WT reference energy. This result is
243 in good agreement with other recent computational studies^{21,22} (**Fig. 3c**). This suggests that
244 the RBD—ACE2 complexes for these three VoCs are stabilized by more intermolecular bonds
245 such as hydrogen or VdW bonds. Several intermolecular contacts were observed to form,
246 break and reform during the simulations (**Fig. 3d**), mostly in the region around RBD residue
247 501, as can be observed in the enlarged regions (**Fig. 3e**).

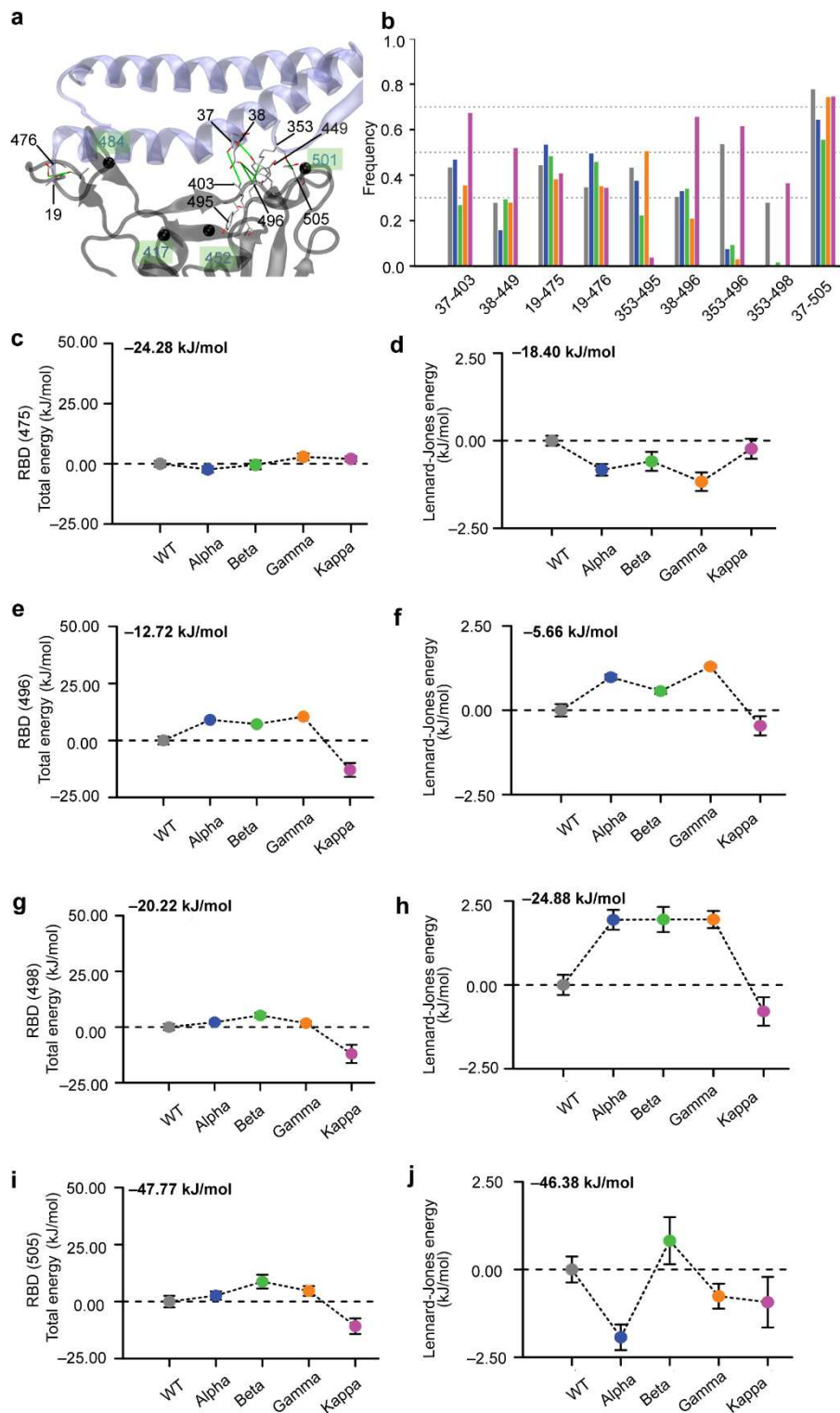
248 Fine energetic analysis of the point mutations revealed important differences between the
249 WT and VoCs (**Fig. 4**). Each individual mutation can influence binding towards ACE2 but can
250 also be associated with local conformational and stability perturbations. Among all mutations,
251 the mutation N501Y, that is common to three mutants (*i.e.* Alpha, Beta and Gamma), seems
252 to have the highest impact in terms of energies. This mutation strongly enhances the
253 interaction between the RBD and ACE2 via new contacts which are correlated with a gain in
254 the Lennard-Jones energy (**Fig. 4j**) of about 10 kJ/mol. The Kappa variant that lacks the N501Y
255 mutation shows similar energy to the WT SARS-CoV-2. The mutation E484K in RBD changes
256 the residue charge from a negative to a positive value and is present in two VoC (*i.e.* Beta and
257 Gamma), while for the Kappa variant, it changes to uncharged glutamine. For this latter VoC,
258 one weak interaction with the positively charged K31 residue in ACE2 appears in the MD

259 simulation (**Fig. 4g**). Same contact is present in WT and Alpha and it vanishes in case of Beta
260 and Gamma, mostly due to the repulsive energy between both positive charged residues in
261 RBD mutant and ACE2 (**Fig. 3d**). The positive charge residue K417 was mutated to an
262 uncharged residue in Beta and Gamma (**Fig. 4a,b**). **Fig. 3d** shows the contact K417-D30 that is
263 found with a higher frequency (>0.7) for WT, Alpha and Kappa, and compatible with a salt
264 bridge. On the other hand, the contact with a mutation N417-D30 has a very low frequency
265 (<0.3) for Beta and even it disappears for the Gamma VoC.



266 **Figure 4 | Energetic analysis of the RBD point mutations through MD simulation.** Total energies (a,c,e,g,i) and
 267 Lennard-Jones (b,d,f,h,j) interaction energies between contact ACE2 and RBD residues 417 (a,b), 452 (c,d), 478
 268 (e,f) 484 (g,h) and 501 (i,j). For ease of comparison, the values have been reset to zero for the WT and the initial
 269 value of the WT is shown at the top left.

270 Furthermore, our analysis provides an additional picture associated with conserved residues
271 in RBD whose chemical environment changes following mutations. The residue Y475 shows
272 no change in total energy along WT and all mutants (**Fig. 5c**). However, the Lennard-Jones
273 energy favors Alpha, Beta and Gamma, over the Kappa mutant (**Fig. 5d**). This is manifested by
274 the increasing contact frequency in Y475-S19 (~ 0.6) and a drop for Gamma and Kappa mutants
275 around 0.4 (**Fig. 5b**). The energy of G496 residue shows the environment of Kappa as more
276 favorable denoted by the lowest total energy, whereas its Lennard-Jones energy seems to
277 fluctuate close to WT energy (**Fig. 5e,f**). For this residue two contacts are obtained (i.e. G496-
278 D38 G496-K353) with high frequency (>0.6) (**Fig. 5b**) which are stabilized by long-range
279 electrostatic interactions. Residue Q498 maintains a contact with K353 in ACE2 for WT and
280 Kappa, while this contact is lost in the other mutants. This effect is correlated by having the
281 local environment with lowest total and Lennard-Jones energies (**Fig. 5g,h**). Finally, Y505-E37
282 is a contact whose strength decreases in Alpha and Beta respect to WT and is recovered for
283 Gamma and Kappa. Remarkably, we observed that for the Kappa variant, two contacts
284 appeared at high frequency with the ACE2 β -hairpin (K353-G496 and K353-Q498) providing a
285 larger and more stable interface between the ACE2 and RBD (**Fig. 5i,j**). We also observed that
286 the majority of contacts are located close to the ACE2 β -hairpin within the RBD-ACE2 interface,
287 which is even more stabilized in the Kappa variant (**Fig. 5a**). This process can be seen as key
288 during spontaneous unbindings or under loading forces in AFM, as it might keep the ACE2
289 anchored on side of the interface for longer times.



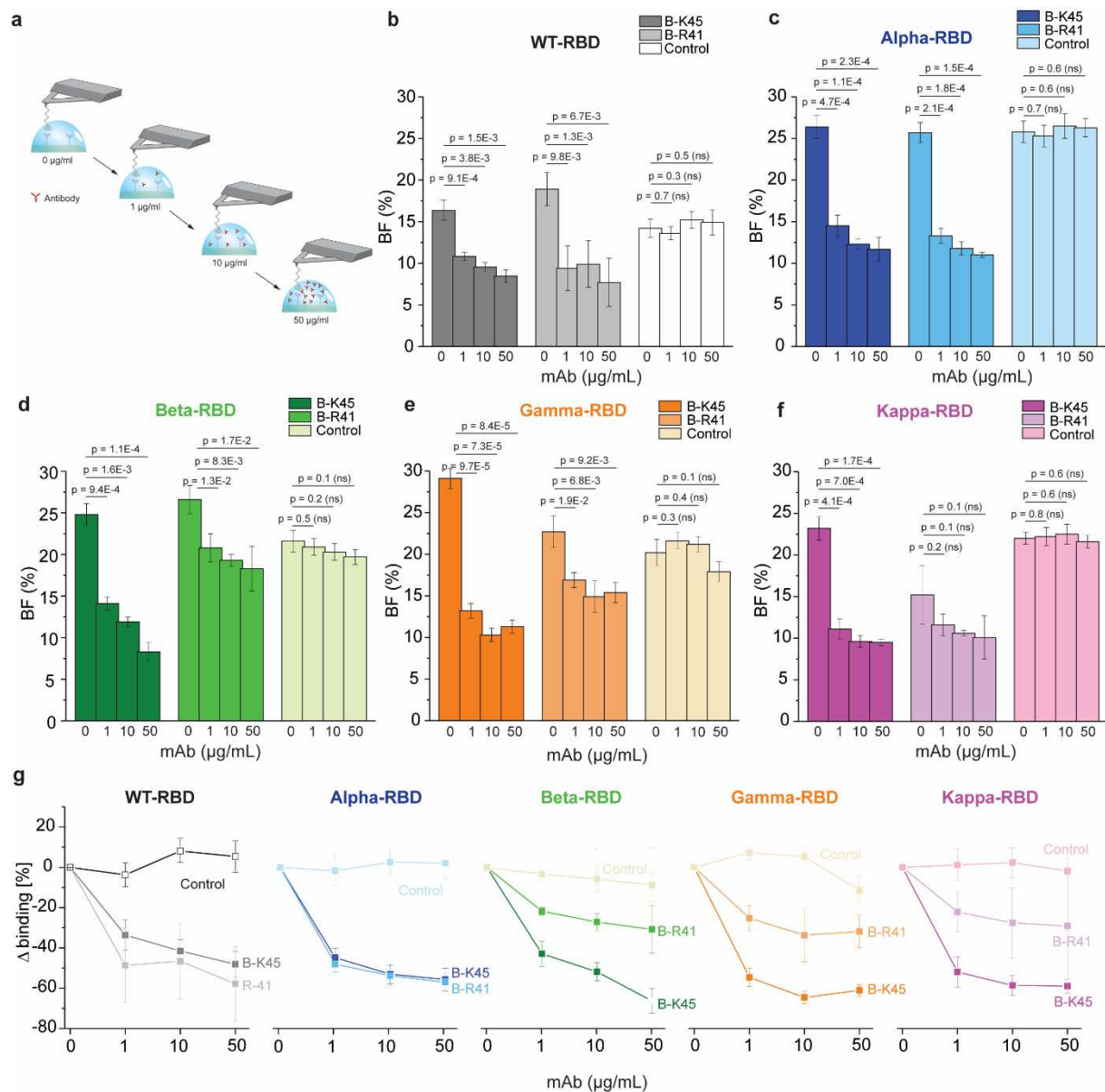
290 **Figure 5| Indirect structural and energetic changes of the conserved residues of the RBD—ACE2 complex due**
 291 **to VoCs point mutations.** (a) Ribbon-like representation of the RBD—ACE2 complex and highlights of the set of
 292 high-frequency contacts (solid green lines) that are formed by RBD conserved residues following mutations
 293 shown in black balls. (b) Average frequency of contacts between RBD and ACE2 molecules. These contacts are
 294 obtained from MD trajectories. Only contacts whose frequencies are larger than 0.3 and their difference to WT
 295 larger than 0.2 are shown. Bottom panels show total energies (c, e, g, i) and Lennard-Jones (d,f,h,j)
 296 interaction energies between contact ACE2 and RBD residues 475 (c,d), 496 (e,f), 498 (g,h) and 505 (i,j). Error bars in energies
 297 are given as standard deviations.

298 **Antibodies targeting RBD of SARS-CoV-2 as potential treatment of COVID-19**

299 Since the S protein has been found to be the primary antigenic epitope on SARS-CoV-2,
300 antibodies directed against this protein can neutralize the ability of the virus to bind and fuse
301 with the target host cell^{25,26}. The traditional neutralization mechanism is to block the receptor-
302 binding site located between RBD and ACE2. Recently, several studies report the use of
303 neutralizing monoclonal antibodies (mAbs) against the RBD region of the S protein^{27,28},
304 rendering them a promising tool to be used as therapeutics against COVID-19. Here, we tested
305 the binding inhibition efficiency of two IgG1 mAbs (B-K45 and B-R41, Diaclone SAS, France)
306 directed against the WT RBD, using our single-molecule force spectroscopy approach (**Fig. 6**),
307 with the goal to understand how they could neutralize the VoCs. As a reference, we first
308 measured the BF between the WT-RBD or variants and the ACE2 receptor without mAb, using
309 a contact time of 250 ms. Then, we injected the mAb at gradually increasing concentrations
310 (1, 10 and 50 $\mu\text{g}/\text{mL}$) and pursued monitoring the BF (**Fig. 6a**). After B-K45 injection, we
311 observed a progressive reduction of the BF as a function of the concentration for all WT and
312 VoCs RBD (**Fig. 6b-f**). As a control for the specific inhibition capability of the mAb, we also
313 tested a control mAb (B-D38, Isotype control IgG1, Diaclone SAS, France). Using this isotype
314 control, we did not observe any specific inhibition confirming that the inhibition with B-K45 is
315 specific. Quantitative comparison of inhibition level among RBDs (**Fig. 6g**) pointed out a BF
316 reduction of >50% already at 1-10 $\mu\text{g}/\text{mL}$ for all the probed RBD-ACE2 interaction pairs,
317 suggesting an IC_{50} (50% inhibitory concentration) in the $\mu\text{g}/\text{mL}$ range. Strikingly, this result
318 shows that B-K45, although obtained from the immunization of mice with the WT-RBD,
319 inhibits even more efficiently the VoCs-RBD binding to ACE2. A different behavior can be
320 noticed for the second tested mAb, B-R41. Here, only binding of RBD WT and the Alpha variant
321 to the ACE2 receptor can be efficiently inhibited (IC_{50} at 1 $\mu\text{g}/\text{mL}$). The other RBD variants

322 (Beta, Gamma, Kappa) are still able to bind to the receptor in the presence of B-R41, however
323 with a 20-30% reduction of the BF. Altogether, our *in vitro* assays at the single-molecule level
324 provide direct evidence that mAbs directed against WT-RBD can also inhibit binding of the
325 tested VoCs. However, as observed for the B-R41 mAb, VoCs can escape from this
326 neutralization, probably as a consequence of the E484 mutation, as the three variants (beta,
327 gamma and kappa) showing a reduced inhibition share this particular mutation.

328



329

330 **Figure 6] Probing antibody efficiency to inhibit binding of the different RBD mutants to ACE2 receptor.**
 331 Efficiency of blocking antibodies is evaluated by measuring the binding frequency of the interaction between
 332 ACE2 and the RBD mutants before and after incubation with the three different monoclonal antibodies (mAb) at
 333 increasing concentration (1-50 µg/ml). **(b-f)** Histograms showing the binding frequency of the interaction
 334 between ACE2 and WT-RBD (b), Alpha-RBD (c), Beta-RBD (d), Gamma-RBD (e) or Kappa-RBD (B.1.617) (f) without
 335 mAb and upon incubation with 1, 10, or 50 µg/ml of two monoclonal anti-RBD (B-K45 and B-R41) or a control
 336 IgG1 isotype mAb. **(g)** Graph showing the reduction of the binding frequency. Data are representative of at least
 337 N = 3 independent experiments (tips and sample) per antibody concentration. P values were determined by two-
 338 sample t-test in Origin. The error bars indicate s.d. of the mean value.

339 DISCUSSION

340 The emergence of SARS-CoV-2 variants of concern across the globe is worrisome, especially
341 as the mutations could result in more transmissible viruses and impair recognition of the virus
342 by human antibody-mediated immunity. To better understand why these point mutations in
343 the SARS-Cov-2 RBD led to the emergence of these variants, we studied how they affect the
344 kinetic and thermodynamic properties towards ACE2 receptor binding. Using a combination
345 of *in vitro* and *in silico* approaches, we linked the energetic properties of RBD-ACE2 complex
346 formation to associated structural changes. By probing the interactions using AFM force
347 spectroscopy (**Fig. 2**), we showed that mutations within the RBD of the different variants led
348 in all cases to higher stability and affinity of the RBD—ACE2 complex. The data obtained here
349 are consistent with a model in which variant spike proteins mediate increased transmissibility,
350 at least in part, by enhancing ACE2 binding affinity^{12,29}.

351 Surprisingly, MD simulations revealed that only the Kappa mutant among all investigated
352 variants show a more stable complex, as pointed out by the total energy extracted from the
353 MD simulations (**Fig. 3b**). However, by looking at interfacial energy, we noticed that the three
354 other VoCs showed a more stable binding interface, with a gain of around 10kJ/mol, stabilized
355 by more intermolecular bonds. Looking at the residue level, a crucial role for the N501Y
356 mutation present in the Alpha, Beta and Gamma variants was identified, resulting in a
357 significant gain in stabilization of the RBD—ACE2 interface. Structurally, RBD residue 501Y,
358 present in all three variants, has a larger phenolic group that makes two additional contacts
359 with ACE2 residues, coordinately stabilizing several segments within the RBD—ACE2 interface.
360 Regarding Kappa variant, mutation of RBD residue 484 (E484Q) plays an important role from
361 energetics point of view. Strikingly, the gain of energy results from long-range Coulomb

362 interactions, establishing an electrostatic bridge at the RBD—ACE2 interface and clamping the
363 central zone of the complex, which limits the possibilities of conformational adjustments
364 during the binding/unbinding process. Taken together, these observations demonstrate that
365 these variants, although having arisen independently, evolve in such a way as to stabilize the
366 contact interface between the RBD and the ACE2 receptor. This evolution appears to be
367 towards hot binding spots making more stable contacts with the termini of the α -helix ACE2
368 receptor encompassing residues [22-57], confirming its great potential as therapeutic target¹⁰.
369 We also noticed that the point mutations in variant RBDs result in structural rearrangement
370 of conserved residues that stabilize more the binding interface.

371 Finally, we also investigated the neutralization mechanism of mAbs at the single-molecule
372 level. We compared two different mAbs and observed that one of those, the B-R41, lost its
373 neutralization potential for the three SARS-CoV-2 variants exhibiting the most stable interface
374 (Beta, Gamma, Kappa). On the opposite, the other mAb (B-K45) shows a similar inhibition
375 efficacy for both, WT and VoCs. As those mAb have been obtained by the immunization of a
376 mouse with the WT-RBD, our results demonstrate at the single-molecule level that new
377 variants will have reduced susceptibility to neutralization by the polyclonal plasma antibodies
378 of some individuals. However, it is tricky to link the loss of neutralization susceptibility to a
379 particular mutation. Nevertheless, we observed that the Alpha variant being neutralized by
380 the B-41 shares the N501Y mutation with other mutant that escape the neutralization. This
381 result is consistent with previous observations which suggest that N501Y mutation is unlikely
382 to greatly affect neutralization by most human plasma, although it could contribute to
383 increased viral titer or enhanced transmissibility^{8,30}.

384 Our mapping reveals broader features of the importance of mutations for RBD binding to the
385 ACE2 receptor that are relevant to the evolution of SARS-CoV-2. It also suggests that there is
386 an important area of future work to understand how viral mutations can impact on the
387 stability of the interface and use this knowledge to develop strategies to robustly counteract
388 viral antigenic evolution.

389 **METHODS**

390 **Protein expression and purification**

391 All antibodies used in the study were developed and purified by Diaclone SAS (France). Anti-
392 RBD mAbs (B-K45 and B-R41) come from immunization of BALB/c mice with WT-RBD protein
393 (Diaclone SAS, 715-H16-0BU). B-D38 (Diaclone, SAS, France) has been used as an isotype
394 control IgG1.

395 **Functionalization of AFM tips**

396 MSCT-D cantilevers (Bruker) were used to probe the interaction between S1 spike
397 glycoprotein subunits (Diaclone SAS, 715-H16-0BU, 715-H24-0BU, 715-H22-0BU, 715-H21-
398 0BU, 715-H20-0BU) and extracellular domain of ACE-2 receptors (Diaclone SAS, 715-H19-
399 0BU). AFM tips were functionalized with the spike proteins using NHS-PEG₂₄-Ph-aldehyde
400 (Broadpharm) linkers as described previously³¹. The cantilevers were rinsed by immersing in
401 chloroform for 10 min and further cleaned by UV-radiation and ozone. Silanization was
402 performed in the gas phase³² by placing the AFM tips in a desiccator with separate vials
403 containing 3-aminopropytriethoxysilane APTES (30 µl) and triethylamine TEA (10 µl). The tips
404 were incubated for 2 hours, following which the desiccator was flushed with argon and left to
405 cure for at least two days. Following amino-functionalization, AFM tips were coupled with
406 flexible PEG linkers. The cantilevers were immersed in a solution of NHS-PEG₂₄-Ph-aldehyde
407 (3.3 mg in 0.5 mL of chloroform) in the presence of triethylamine (30 µl). After 2 hours of
408 incubation at room temperature, the cantilevers were thoroughly washed with chloroform
409 three times and dried under nitrogen.

410 For AFM tips functionalized with RBD proteins, 50 µL of protein solution (0.1 mg/ml in PBS pH
411 7.4) was added to the cantilevers placed Parafilm inside a Petridish. To this, sodium

412 cyanoborohydride NaCNBH_3 (1 μL of 1 M stock solution) was added and was kept for 1 hour
413 at room temperature. Then, ethanolamine hydrochloride (2.5 μL of 1 M stock solution, pH 8.0)
414 was added to block the free aldehyde groups on the AFM cantilever. Subsequently, the AFM
415 tips were washed three times with PBS buffer and used immediately for the experiments.

416 **Preparation of ACE-2 coated model surfaces**

417 ACE-2 protein (Diacclone, SAS, 715-H19-0BU) was immobilized on gold-coated surfaces using
418 NHS-EDC chemistry. Gold-coated surfaces were rinsed with ethanol, dried under nitrogen,
419 cleaned for 15 min by UV-ozone treatment and incubated overnight in solution containing
420 alkanethiol (99% 11-mercapto-1-undecanol 1 mM (Sigma Aldrich) and 1% 16-
421 mercaptohexadecanoic acid 1 mM (Sigma Aldrich) in ethanol). Resultant surfaces were
422 washed with ethanol, dried under a gentle stream of nitrogen, and immersed in a solution 25
423 mg mL^{-1} of dimethylaminopropyl carbodiimide (EDC) and 10 mg mL^{-1} of N-hydroxy
424 succinimide (NHS). Finally, the chemically activated samples were incubated with ACE-2
425 protein (25 μL , 0.1 mg mL^{-1} in PBS, pH 7.4) on parafilm for 30 min and washed with PBS buffer
426 and used on the same day.

427 **FD-based AFM on model surfaces**

428 FD-based AFM on model surfaces was performed at room temperature in PBS using
429 functionalized MSCT probes (Bruker, nominal spring constant of 0.030 N/m and actual spring
430 constants measured prior to the experiment using thermal tune method³³). A Bruker Nano8
431 operated in force-volume (contact) mode in fluid (Nanoscope software v9.1) was used for the
432 determination of kinetic on-rate (measuring the binding probability for different contact times
433 of 0, 50, 100, 150, 250, 500, and 1000 ms). For each force map, a scan size of 5 μm , a set point
434 force of 500 pN, resolution of 32 \times 32 pixels and a line frequency of 1 Hz were used.

435 A JPK Force Robot 300 AFM was used to measure the loading rates and disruption forces by
436 DFS analysis (using a constant approach speed of 1 $\mu\text{m/s}$ and variable retraction speeds of 0.1,
437 0.2, 1, 5, 10, and 20 $\mu\text{m/s}$). DFS data were extracted using the JPK Data Analysis software (JPK)
438 and further analyzed using Origin software (OriginLab, version 2019) to fit histograms of
439 rupture force distributions for distinct LR ranges, and to apply various force spectroscopy
440 models^{10,13,14}. For kinetic on-rate analysis, the binding probability (fraction of curves showing
441 binding events) was determined at a certain contact time (t) (the time the tip is in contact with
442 the surface). Those data were fitted and K_D calculated as described previously³⁴.

443 In brief, the relationship between interaction time (τ) and BP is described by the following
444 equation:

$$445 \quad BP = A \times \left[1 - \exp\left(\frac{-(t - t_0)}{t}\right) \right]$$

446 where A is the maximum BP and t_0 the lag time. Origin software is used to fit the data and
447 extract τ . In the next step, k_{on} was calculated by the following equation, with r_{eff} the radius of
448 the sphere, n_b the number of binding partners, and N_A the Avogadro constant

$$449 \quad k_{on} = \frac{\frac{1}{2} \cdot 4\pi r_{eff}^3 \cdot N_A}{3\eta_b \tau}$$

450 The effective volume V_{eff} ($4\pi r_{eff}^3$) represents the volume in which the interaction can take
451 place.

452 **Antibody inhibition assays**

453 To study the influence of antibodies on the binding affinity between RBD of different mutants
454 and the ACE-2 receptor, binding probabilities were measured before and after incubation with
455 different concentrations (1, 10 and 50 $\mu\text{g mL}^{-1}$) of three different antibodies (xx). Briefly, three

456 force-volume maps were recorded on three different areas as described previously in the
457 absence of any antibody (i.e., force-volume mode, 1 μ m/s approach and retraction speed, map
458 size of 5 μ m, threshold force of 500 pN, 32 \times 32 pixels, 512 samples/line, frequency of 1Hz, and
459 contact time of 250 ms on surface). Thereafter, antibodies were added to the fluid cell and
460 three maps were recorded for each concentration.

461 **Modeling of SARS-CoV-2 RBD—ACE2 complex and RBD mutants**

462 The human angiotensin-converting enzyme 2 (ACE2) is recognized by the receptor binding
463 domain (RBD) of SARS-CoV2 spike (S) protein and together they form a protein complex (PDB
464 code 6M0J for WT)³⁵. The RBD and ACE2 comprise residues 333 to 526 and 19 to 615
465 respectively. The models in this work retain the Zn²⁺ ions which are electrostatically bonded
466 to residues HIS 374, HIS 378, GLU 402 in ACE2. The protocol to model mutations in the RBD is
467 made by replacing amino acids in an energetic favorable conformation by UCSF Chimera³⁶ and
468 Dunbrack rotamer library. The Alpha variant includes only one mutation (i.e. N501Y) in their
469 RBD domain, while Beta has 3 mutations (i.e. K417N, E484K, and N501Y). Also, Gamma variant
470 has also 3 mutations (i.e. K417T, E484K, and N501Y) while the Kappa variant present only 2
471 mutations (i.e. L452R and E484Q) in their RBD domain.

472 **All-atom MD simulation**

473 The molecular package GROMACS²² was used to carry out all-atom MD simulations. The
474 protein, water and ions were modeled by CHARMM36m³⁷ force-field. Solvent employed the
475 TIP3P water model. The WT and VoCs RBD in complex with ACE2 were optimized using
476 standard energy minimization (1500 steps) and conjugate gradient (500 steps) algorithms
477 available in GROMACS. Also, the equilibration of systems was done in the NVT and NPT
478 ensemble. The v-rescaled thermostat was used to maintain the temperature constant in the

479 NVT ensemble for 10 ps and the Berendsen barostat in the NPT ensemble for 100 ps. Later the
480 production was carried out in the NVT ensemble. The RBD—ACE2 complex was initially placed
481 at the center of the simulation box which was solvated in 12 Å octahedral water shell. MD
482 trajectories were checked for atomic clashes. All simulations used 0.15 mol/L of NaCl
483 molecules. We employed a 2 fs timestep for every MD simulation. During pre-production
484 restraints of 41.84 kJ mol⁻¹ Å⁻² were applied on the backbone of the complex. Last 50 ns of
485 unconstrained MD simulation in the NVT ensemble using the Parrinello-Rahman barostat
486 maintained the system at 300 K and 1 bar. The production runs include 5 replicas for the WT
487 and 4 variants. Each replica was run by 250 ns. Thus, we got a cumulative time of 1.5 μs for
488 each system. Trajectories were saved every 40 ps/frame, which were used in further analysis
489 (see below).

490 **Energetics and contact analysis of the RBD—ACE2 complex for WT and mutants**

491 The energetic analysis of RBD—ACE2 interface employs the gmx energy utility in GROMACS.
492 We calculate the electrostatic and Van der Waals energies originated by the Coulomb
493 interaction and the Lennard-Jones potential respectively for each replica. The total number of
494 frames used for the analysis equals 54005 in each 1.5 μs MD trajectory. These energies
495 consider amino acids residue in RBD and ACE2 that constitute the interface. In addition, we
496 employ our contact analysis methodology already validated in several protein complexes^{38,39}
497 and recently validated for the study of the S protein^{40,41}. The contact maps are based on the
498 OV+rCSU approach⁴². We obtained from our trajectories 19377 contact maps which have been
499 employed in the analysis of the frequency per contact.

500

501

502 **DATA AVAILABILITY**

503 The Source data underlying Figs. 2-6 and Supplementary Fig. 1 are provided as a Source Data
504 file. All other relevant data are available from the corresponding authors upon reasonable
505 request.

506 **ACKNOWLEDGEMENTS**

507 This work was supported by the Université catholique de Louvain, the Foundation Louvain,
508 and the Fonds National de la Recherche Scientifique (FRS-FNRS). This project received funding
509 from the European Research Council under the European Union's Horizon 2020 research and
510 innovation program (grant agreement No. 758224) and from the FNRS-Welbio (Grant # CR-
511 2019S-01). The funders had no role in study design, data collection and analysis, decision to
512 publish, or preparation of the paper. M.K. and D.A. are postdoctoral researcher and research
513 associate at the FNRS, respectively. A.P. acknowledges financial support from the National
514 Science Centre, Poland, under grant 2017/26/D/NZ1/00466, the grant MAB PLUS/11/2019
515 from the Foundation for Polish Science, and also computational resources were supported by
516 the PL-GRID infrastructure. Cartoons in Figures 1a–d and 6a were created with
517 BioRender.com.

518 **AUTHOR CONTRIBUTIONS**

519 M.K., A.R. and D.A. conceived the project, planned the experiments, and analyzed the data.
520 M.K., A.R. and B.J. conducted the AFM experiments. R.A.M.d.S. and A.P. designed, performed
521 and analyzed the MD simulation. All authors wrote the paper.

522 **COMPETING INTERESTS**

523 The authors declare no competing interests.

- 525 1 Bonaventura, A., Vecchié, A., Dagna, L., Martinod, K., Dixon, D. L., Van Tassell, B. W., . . . Levi,
526 M. Endothelial dysfunction and immunothrombosis as key pathogenic mechanisms in COVID-
527 19. *Nature Reviews Immunology* **21**, 319-329 (2021).
- 528 2 Schultze, J. L. & Aschenbrenner, A. C. COVID-19 and the human innate immune system. *Cell*
529 (2021).
- 530 3 Dallmeier, K., Meyfroidt, G. & Neyts, J. COVID-19 and the intensive care unit: vaccines to the
531 rescue. *Intensive Care Med.*, 1-4 (2021).
- 532 4 Krause, P. R., Fleming, T. R., Longini, I. M., Peto, R., Briand, S., Heymann, D. L., . . . Ropero, A.-
533 M. SARS-CoV-2 Variants and Vaccines. *New England Journal of Medicine* (2021).
- 534 5 Zhu, N., Zhang, D., Wang, W., Li, X., Yang, B., Song, J., . . . Tan, W. A Novel Coronavirus from
535 Patients with Pneumonia in China, 2019. *N. Engl. J. Med.* **382**, 727-733,
536 doi:10.1056/NEJMoa2001017 (2020).
- 537 6 Shu, Y. & McCauley, J. GISAID: Global initiative on sharing all influenza data - from vision to
538 reality. *Euro Surveill.* **22**, doi:10.2807/1560-7917.Es.2017.22.13.30494 (2017).
- 539 7 Ho, D., Wang, P., Liu, L., Iketani, S., Luo, Y., Guo, Y., . . . Huang, Y. Increased Resistance of SARS-
540 CoV-2 Variants B.1.351 and B.1.1.7 to Antibody Neutralization. *Res Sq*, doi:10.21203/rs.3.rs-
541 155394/v1 (2021).
- 542 8 Greaney, A. J., Loes, A. N., Crawford, K. H. D., Starr, T. N., Malone, K. D., Chu, H. Y. & Bloom, J.
543 D. Comprehensive mapping of mutations in the SARS-CoV-2 receptor-binding domain that
544 affect recognition by polyclonal human plasma antibodies. *Cell Host Microbe* **29**, 463-
545 476.e466, doi:10.1016/j.chom.2021.02.003 (2021).
- 546 9 Zhu, X., Mannar, D., Srivastava, S. S., Berezuk, A. M., Demers, J. P., Saville, J. W., . . .
547 Subramaniam, S. Cryo-electron microscopy structures of the N501Y SARS-CoV-2 spike protein
548 in complex with ACE2 and 2 potent neutralizing antibodies. *PLoS Biol.* **19**, e3001237,
549 doi:10.1371/journal.pbio.3001237 (2021).
- 550 10 Yang, J., Petitjean, S. J. L., Koehler, M., Zhang, Q., Dumitru, A. C., Chen, W., . . . Alsteens, D.
551 Molecular interaction and inhibition of SARS-CoV-2 binding to the ACE2 receptor. *Nature*
552 *communications* **11**, 1-10 (2020).
- 553 11 Johnson, B. A., Xie, X., Bailey, A. L., Kalveram, B., Lokugamage, K. G., Muruato, A., . . .
554 Menachery, V. D. Loss of furin cleavage site attenuates SARS-CoV-2 pathogenesis. *Nature* **591**,
555 293-299, doi:10.1038/s41586-021-03237-4 (2021).
- 556 12 Khan, A., Zia, T., Suleman, M., Khan, T., Ali, S. S., Abbasi, A. A., . . . Wei, D. Q. Higher infectivity
557 of the SARS-CoV-2 new variants is associated with K417N/T, E484K, and N501Y mutants: An
558 insight from structural data. *J. Cell. Physiol.*, doi:10.1002/jcp.30367 (2021).
- 559 13 Newton, R., Delguste, M., Koehler, M., Dumitru, A. C., Laskowski, P. R., Müller, D. J. & Alsteens,
560 D. Combining confocal and atomic force microscopy to quantify single-virus binding to
561 mammalian cell surfaces. *Nat. Protoc.* **12**, 2275 (2017).
- 562 14 Alsteens, D., Newton, R., Schubert, R., Martinez-Martin, D., Delguste, M., Roska, B. & Muller,
563 D. J. Nanomechanical mapping of first binding steps of a virus to animal cells. *Nat. Nanotechnol*
564 **12**, 177-183, doi:10.1038/nnano.2016.228 (2017).
- 565 15 Bell, G. I. Models for the specific adhesion of cells to cells. *Science* **200**, 618-627 (1978).
- 566 16 Evans, E., Ritchie, K. & Merkel, R. Sensitive force technique to probe molecular adhesion and
567 structural linkages at biological interfaces. *Biophys. J.* **68**, 2580-2587, doi:10.1016/s0006-
568 3495(95)80441-8 (1995).
- 569 17 Koehler, M., Aravamudhan, P., Guzman-Cardozo, C., Dumitru, A. C., Yang, J., Gargiulo, S., . . .
570 Alsteens, D. Glycan-mediated enhancement of reovirus receptor binding. *Nature*
571 *Communications* **10**, 1-14 (2019).
- 572 18 Delguste, M., Zeippen, C., Machiels, B., Mast, J., Gillet, L. & Alsteens, D. Multivalent binding of
573 herpesvirus to living cells is tightly regulated during infection. *Sci. Adv.* **4**, eaat1273 (2018).

- 574 19 Rankl, C., Kienberger, F., Wildling, L., Wruss, J., Gruber, H. J., Blaas, D. & Hinterdorfer, P.
575 Multiple receptors involved in human rhinovirus attachment to live cells. *Proc. Natl. Acad. Sci.*
576 *U. S. A.* **105**, 17778-17783, doi:10.1073/pnas.0806451105 (2008).
- 577 20 Sieben, C., Kappel, C., Zhu, R., Wozniak, A., Rankl, C., Hinterdorfer, P., . . . Herrmann, A.
578 Influenza virus binds its host cell using multiple dynamic interactions. *Proc. Natl. Acad. Sci. U.*
579 *S. A.* **109**, 13626-13631 (2012).
- 580 21 Li, W., Moore, M. J., Vasilieva, N., Sui, J., Wong, S. K., Berne, M. A., . . . Greenough, T. C.
581 Angiotensin-converting enzyme 2 is a functional receptor for the SARS coronavirus. *Nature*
582 **426**, 450-454 (2003).
- 583 22 Abraham, M. J., Murtola, T., Schulz, R., Páll, S., Smith, J. C., Hess, B. & Lindahl, E. GROMACS:
584 High performance molecular simulations through multi-level parallelism from laptops to
585 supercomputers. *SoftwareX* **1**, 19-25 (2015).
- 586 23 Mehdipour, A. R. & Hummer, G. Dual nature of human ACE2 glycosylation in binding to SARS-
587 CoV-2 spike. *Proceedings of the National Academy of Sciences* **118**, e2100425118,
588 doi:10.1073/pnas.2100425118 (2021).
- 589 24 Qiao, B. & Olvera de la Cruz, M. Enhanced Binding of SARS-CoV-2 Spike Protein to Receptor by
590 Distal Polybasic Cleavage Sites. *ACS Nano* **14**, 10616-10623, doi:10.1021/acsnano.0c04798
591 (2020).
- 592 25 Klasse, P. J. & Moore, J. P. Antibodies to SARS-CoV-2 and their potential for therapeutic passive
593 immunization. *eLife* **9**, e57877, doi:10.7554/eLife.57877 (2020).
- 594 26 Valdez-Cruz, N. A., García-Hernández, E., Espitia, C., Cobos-Marín, L., Altamirano, C., Bando-
595 Campos, C. G., . . . Trujillo-Roldán, M. A. Integrative overview of antibodies against SARS-CoV-
596 2 and their possible applications in COVID-19 prophylaxis and treatment. *Microbial Cell*
597 *Factories* **20**, 88, doi:10.1186/s12934-021-01576-5 (2021).
- 598 27 Taylor, P. C., Adams, A. C., Hufford, M. M., de la Torre, I., Winthrop, K. & Gottlieb, R. L.
599 Neutralizing monoclonal antibodies for treatment of COVID-19. *Nature Reviews Immunology*
600 **21**, 382-393, doi:10.1038/s41577-021-00542-x (2021).
- 601 28 Min, L. & Sun, Q. Antibodies and Vaccines Target RBD of SARS-CoV-2. *Front Mol Biosci* **8**,
602 671633-671633, doi:10.3389/fmolb.2021.671633 (2021).
- 603 29 Ramanathan, M., Ferguson, I. D., Miao, W. & Khavari, P. A. SARS-CoV-2 B.1.1.7 and B.1.351
604 spike variants bind human ACE2 with increased affinity. *The Lancet Infectious Diseases* **21**,
605 1070, doi:10.1016/S1473-3099(21)00262-0 (2021).
- 606 30 Kidd, M., Richter, A., Best, A., Mirza, J., Percival, B., Mayhew, M., . . . McNally, A. S-variant
607 SARS-CoV-2 is associated with significantly higher viral loads in samples tested by
608 ThermoFisher TaqPath RT-QPCR. *medRxiv*, 2020.2012.2024.20248834,
609 doi:10.1101/2020.12.24.20248834 (2020).
- 610 31 Wildling, L., Unterauer, B., Zhu, R., Rupprecht, A., Haselgrübler, T., Rankl, C., . . . Pohl, E. E.
611 Linking of sensor molecules with amino groups to amino-functionalized AFM tips. *Bioconjugate*
612 *chemistry* **22**, 1239-1248 (2011).
- 613 32 Ebner, A., Hinterdorfer, P. & Gruber, H. J. Comparison of different aminofunctionalization
614 strategies for attachment of single antibodies to AFM cantilevers. *Ultramicroscopy* **107**, 922-
615 927, doi:10.1016/j.ultramic.2007.02.035 (2007).
- 616 33 Butt, H.-J. & Jaschke, M. Calculation of thermal noise in atomic force microscopy.
617 *Nanotechnology* **6**, 1 (1995).
- 618 34 Rankl, C., Wildling, L., Neundlinger, I., Kienberger, F., Gruber, H., Blaas, D. & Hinterdorfer, P. in
619 *Atomic Force Microscopy in Biomedical Research* 197-210 (Springer, 2011).
- 620 35 Lan, J., Ge, J., Yu, J., Shan, S., Zhou, H., Fan, S., . . . Wang, X. Structure of the SARS-CoV-2 spike
621 receptor-binding domain bound to the ACE2 receptor. *Nature*, doi:10.1038/s41586-020-2180-
622 5 (2020).
- 623 36 Pettersen, E. F., Goddard, T. D., Huang, C. C., Couch, G. S., Greenblatt, D. M., Meng, E. C. &
624 Ferrin, T. E. UCSF Chimera—a visualization system for exploratory research and analysis. *J.*
625 *Comput. Chem.* **25**, 1605-1612 (2004).

626 37 Huang, J., Rauscher, S., Nawrocki, G., Ran, T., Feig, M., De Groot, B. L., . . . MacKerell, A. D.
627 CHARMM36m: an improved force field for folded and intrinsically disordered proteins. *Nat.*
628 *Methods* **14**, 71-73 (2017).

629 38 Chwastyk, M., Bernaola, A. P. & Cieplak, M. Statistical radii associated with amino acids to
630 determine the contact map: Fixing the structure of a type I cohesin domain in the *Clostridium*
631 *thermocellum* cellulosome. *Phys. Biol.* **12**, 046002 (2015).

632 39 Senapati, S., Poma, A. B., Cieplak, M., Filipek, S. & Park, P. S. H. Differentiating between inactive
633 and active states of rhodopsin by atomic force microscopy in native membranes. *Anal. Chem.*
634 **91**, 7226-7235 (2019).

635 40 Moreira, R. A., Chwastyk, M., Baker, J. L., Guzman, H. V. & Poma, A. B. Quantitative
636 determination of mechanical stability in the novel coronavirus spike protein. *Nanoscale* **12**,
637 16409-16413 (2020).

638 41 Moreira, R. A., Guzman, H. V., Boopathi, S., Baker, J. L. & Poma, A. B. Characterization of
639 structural and energetic differences between conformations of the SARS-CoV-2 spike protein.
640 *Materials* **13**, 5362 (2020).

641 42 Poma, A. B., Cieplak, M. & Theodorakis, P. E. Combining the MARTINI and structure-based
642 coarse-grained approaches for the molecular dynamics studies of conformational transitions
643 in proteins. *J. Chem. Theory Comput.* **13**, 1366-1374 (2017).

644

Supplementary Files

This is a list of supplementary files associated with this preprint. Click to download.

- [VoCsSI.pdf](#)